processes

MDPI

Article

Data-Driven Co-Optimization of Multiple Structural Parameters for the Combustion Chamber in a Coke Oven with a Multi-Stage Air Supply System

Yuan Shan [1,2], Chen Yang [1], Xinyu Ning [3], Mingdeng Wang [2], Yaopeng Li [1,*], Ming Jia [1,*] and Hong Liu [1]

[1] Key Laboratory of Ocean Energy Utilization and Energy Conservation of Ministry of Education, Dalian University of Technology, Dalian 116024, China; shanyuan@mail.dlut.edu.cn (Y.S.); yangchen3244@mail.dlut.edu.cn (C.Y.); hongliu@dlut.edu.cn (H.L.)
[2] ACRE Coking & Refractory Engineering Consulting Corporation (Dalian), MCC, Dalian 116085, China; wangmingdeng@acre.com.cn
[3] School of Engineering and Physical Science, University of Lincoln, Lincoln LN6 7TS, UK; 19774527@students.lincoln.ac.uk
* Correspondence: liyaopeng@dlut.edu.cn (Y.L.); jiaming@dlut.edu.cn (M.J.)

Abstract

Driven by the urgent reduction in industrial energy consumption and nitrogen oxide (NO_x) emissions, numerical simulation becomes a significant tool to understand the internal working process and optimize the structure of the combustion chamber in coke oven. However, conventional numerical simulation is computationally expensive and impractical for real-time monitoring or multi-parameter optimization. To address this challenge, this study proposes a novel parameter fusion convolutional network (PFCN) to rapidly reconstruct the spatial temperature distribution in the combustion chamber of a coke oven. The key innovation of PFCN is its dual-stream encoding mechanism, which processes structural parameters (1×5 vector) and spatial coordinates (25×200 matrix) separately via dedicated encoders, followed by a cross-modal fusion to effectively integrate these heterogeneous inputs. Furthermore, a support vector machine (SVM) is coupled downstream of the PFCN to estimate the exhaust NO_x emissions based on the predicted physical information. This coupled PFCN–SVM framework allows universal applicability across different combustion chamber configurations. Based on this framework, parametric influence analysis and co-optimization of five key structural parameters are conducted for a three-stage air-supply coke oven. The results reveal that both the air staging ratio and staging height significantly affect combustion performance. Compared to the basecase, the optimized design simultaneously improves temperature homogeneity by 15.2% and reduces NO_x emissions by 8%, with negligible computational cost. This integrated data-driven approach demonstrates considerable potential for combustion chamber optimization, transient process predictions, multi-physics coupling analyses, and online control implementations.

Keywords: coke oven combustion chamber; temperature uniformity; nitrogen oxide (NO_x) emissions; parameter fusion convolutional network (PFCN); support vector machine (SVM)

check for updates

Academic Editor: Andrey Voshkin

Received: 21 October 2025
Revised: 14 November 2025
Accepted: 19 November 2025
Published: 26 November 2025

Citation: Shan, Y.; Yang, C.; Ning, X.; Wang, M.; Li, Y.; Jia, M.; Liu, H. Data-Driven Co-Optimization of Multiple Structural Parameters for the Combustion Chamber in a Coke Oven with a Multi-Stage Air Supply System. *Processes* **2025**, *13*, 3818. https://doi.org/10.3390/pr13123818

Copyright: © 2025 by the authors. Licensee MDPI, Basel, Switzerland. This article is an open access article distributed under the terms and conditions of the Creative Commons Attribution (CC BY) license (https://creativecommons.org/licenses/by/4.0/).

1. Introduction

Coke is one of the three fundamental materials for iron production, yet its energy-intensive production poses a significant challenge for carbon peak commitments. Within coking systems, the combustion chamber serves as an important energy conversion apparatus for coking [1], where the enhancement of the combustion process inside the combustion

chamber is crucial for shortening the coking process and improving energy utilization [2,3]. However, the optimization of the combustion process is difficult due to the complexity of the combustion system. The vertical temperature gradients within the combustion chamber induce stratified coking, which degrades the uniformity of coke quality and increases the energy wastage [4]. Additionally, the high combustion temperature causes unacceptable nitrogen oxide (NO_x) emissions, which becomes a heavy burden for aftertreatment systems [5].

In response to the above issues, the moderate and intense low-oxygen dilution (MILD) combustion has been developed [6,7]. This technology achieves ultra-low NOx and carbon monoxide (CO) emissions, homogeneous temperature distribution, and enhanced fuel flexibility by sustaining reactions in highly diluted, high-temperature oxidizer streams. Consequently, air staging systems are currently integrated into modern combustion chamber designs to achieve the MILD combustion regime [3]. Xu et al. [8] implemented a novel structure of heating flue to feature MILD combustion, and lower combustion temperature and less formation of thermal NO_x in heating flues were observed. Lyu et al. [9] investigated the effects of nozzle arrangement on the flame structure and combustion temperature in a coke oven with a multi-stage air/gas supply system. When the secondary gas nozzle was installed in the center of the combustion chamber, the diffusion of the char oxidation reactions into the upper low-oxygen space facilitated flameless combustion, resulting in a more uniform temperature distribution.

Although the above results confirm the effectiveness of air staging systems in improving temperature uniformity and reducing NO_x emissions in coke ovens, the introduction of multi-stage air supply accordingly increases the number of geometric parameters that need to be optimized, thereby increasing the complexity of optimizing heating flue configurations [10]. However, the experimental optimization remains constrained by the industrial-scale and high retrofit costs [11]. Computational fluid dynamics (CFD) simulation has emerged as an indispensable tool for performing multi-dimensional analyses of combustion kinetics, fluid dynamics, and heat transfer processes [12,13], providing valuable insights into reactant mixing, flame structure, and pollutant formation. Gamrat et al. [14] numerically studied the effect of air staging on NO_x reduction in a coke oven battery and found that 20% external flue gas recirculation resulted in a 50% reduction in NO_x. Yan et al. [15] numerically explored the effects of the distance between staged air inlets on vertical temperature homogeneity by designing five cases, achieving a 60% improvement in vertical heating uniformity through optimization.

Although numerical simulation can provide a comprehensive understanding and optimization for the combustion chamber of coke ovens, its practical implementation is often constrained by prohibitively high computational costs due to the large-scale computational domain. Recently, machine learning (ML) has become a widely recognized and powerful data-driven technique, which is capable of deriving valuable insights and patterns from intricate datasets. This capability underpins its extensive application across diverse fields, such as production control [16,17], scientific exploration [18,19], and numerical simulation [20,21]. Yang et al. [22] developed an ML model using experimentally validated CFD datasets to predict the concentrations of H_2 and CH_4 in the raw coke oven gas, and the key parameters affecting the concentrations of both species were identified. Bhatt and Shrivastava [6] systematically reviewed the application of artificial neural networks (ANNs) in the performance prediction of internal combustion engines, and the advantages of ANN in reducing experimental time and cost were explained in detail. Yang et al. [23] implemented a graph neural network (GNN) for temperature field reconstruction in a steel-rolling reheating furnace. After introducing the process parameters as model inputs and considering the interactions among field nodes, accurate prediction of the temperature spatial distri-

bution within the reheating furnace was realized. Xue et al. [24] proposed a prediction framework based on gradient-descent-driven neural networks, which leverages sparse measurement points to enable online reconstruction of three-dimensional temperature fields in coal-fired boilers. Liu et al. [25] designed residual spatio-temporal convolutional neural networks (RST-CNNs) to capture the dynamic evolution of temperature fields within the thermoelectric coupling processes of mineral electric furnaces. Subsequent research has progressively extended to multi-physics collaborative prediction. For instance, Yang et al. [26] employed a hybrid model combining a spatial autoencoder with a long short term memory network (LSTM) to dynamically predict combustion flame behavior and subsequently forecast pollutant emissions. Strässle et al. [27] successfully predicted the turbulent flame temperature and identified the flame front by establishing a U-net network using flame image data obtained from combustion experiments.

The rapid prediction capability of machine learning models not only facilitates a deep understanding of the internal working process but also enables efficient multi-parameter optimization. Wang et al. [28] introduced a reinforcement learning-based agent that utilizes power plant operational data to optimize the combustion process to simultaneously improve thermal efficiency and NO_x emissions. Zhang et al. [29] successfully predicted the thermal efficiency and soot emissions of biodiesel-hydrogen blended fuel engines using a support vector machine (SVM) model, achieving collaborative optimization through integration with the NSGA-II algorithm. Most recently, Ren et al. [30] augmented a complex CNN with transposed convolution and interpolation modules to effectively leverage limited boiler operational and temperature measurement data for reconstructing the cross-sectional temperature field inside the boiler, thereby enabling real-time guidance for operational parameter adjustment.

According to the literature review, the integration of air staging systems in coke ovens represents a critical advancement for meeting the future energy efficiency targets and more stringent emission standards. However, the experimental or CFD-based optimization of multi-stage air supply systems remains challenging due to the industrial-scale computational domain and long simulation time. Although ML offers considerable potential for accelerating optimization processes, it mainly focuses on performance indicators, such as thermal efficiency, emission products, etc. The accurate reconstruction of spatial temperature fields for different combustion chamber structures in coke ovens remains a significant challenge for ML models. This difficulty arises from the highly complex multi-physics interactions involving chemical reactions, turbulent flow, and heat transfer, which are further complicated by introducing the variations in the coke oven combustion chamber structure.

To address this issue, a convolutional network is developed in this work for rapid prediction of temperature fields. However, due to the difference in data structure and dimensionality between structural and coordinate parameters, conventional single-architecture network (e.g., CNN) cannot process the heterogeneous inputs. Accordingly, a dual-stream encoder architecture, termed the parameter fusion convolutional network (PFCN), is developed by using multi-layer perceptron (MLP) and CNN in this study, which can avoid feature interference and data size dependence. This design separately processes structural parameters and spatial coordinates as network inputs, including inlet spacing, air staging ratio, staging height, exhaust gas recirculation rate, and x-z plane coordinate parameters of the combustion chamber. Then the extracted scalar and geometric features undergo cross-modal fusion via a feature integration module to achieve both precise identification of small-sample characteristics and accurate prediction of the temperature field. Since NO_x formation is closely related to the combustion temperature, an SVM is trained based on the predicted temperature distributions to estimate the level of exhaust NO_x emissions. After validating both models, the integrated PFCN-SVM framework is used to co-optimize

five structural parameters of the combustion chamber via a genetic algorithm. This integrated approach not only achieves enhancements of both temperature uniformity and NO_x suppression but also significantly reduces computational cost. By coupling numerical simulation and data-driven approach, a paradigm shift in coke oven design is established, which is of great significance for accelerating the process of improving energy efficiency and reducing exhaust emissions in industrial coke ovens.

2. Materials and Methods

The overall research framework of this study is illustrated in Figure 1. To enable rapid prediction of the working process in the combustion chamber, the PFCN model is trained based on CFD simulation results. Then the key temperature metrics are extracted from the PFCN predictions and utilized as inputs to an SVM model for NO_x emissions prediction. Following the validation of both the PFCN and SVM models, they are coupled with a genetic algorithm to optimize multiple structural parameters of combustion chambers, achieving improvement in both temperature uniformity and NO_x emissions. Finally, the optimized design is validated against the CFD simulation to further verify the reliability of the PFCN-SVM framework through iterative optimization.

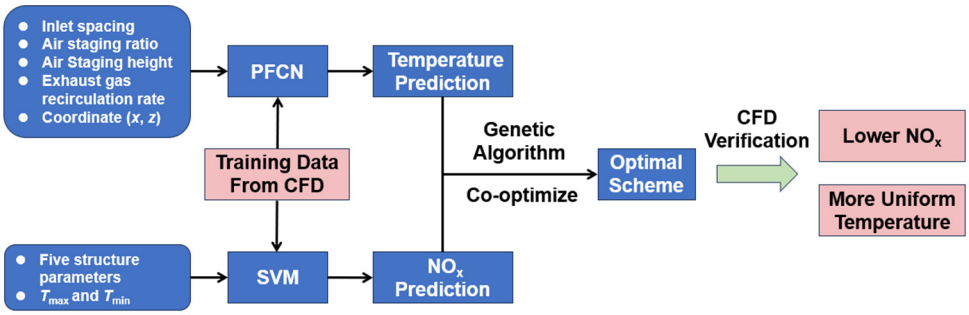


Figure 1. Overall research framework of this study.

2.1. Physical Models

A coke oven system primarily comprises combustion chambers and coking chambers arranged alternately and stacked vertically above regenerators. As shown in Figure 2, each combustion chamber is divided into ascending and descending flues, separated by silica brick walls in a twin-flue configuration. Fuel and air are independently supplied at the bottom through their respective channels. They mix and burn in the ascending flues, and the high-temperature flue gases subsequently flow into the descending flues through the crossing holes. To recover waste heat from exhaust gases for preheating the intake air, the gas flow direction is periodically reversed by alternating the roles of the ascending and descending flues. Furthermore, a vertical cross-section through the gas inlet in the ascending flue is created for predicting the temperature distribution, where this section can accurately represent the thermal profile across the entire combustion chamber under various operating conditions.

The structural parameters of the studied combustion chamber are listed in Table 1, which is designed by ACRE Coking & Refractory Engineering Consulting Corporation (Dalian) in China. The heating flues feature a rectangular cross-section with dimensions of 898 mm in length, 350 mm in width, and 5811 mm in height. The wall thickness is 150 mm for the flue wall and 95 mm for the coke oven wall. The fuel inlet has a diameter of 50 mm, while the air inlet measures 120 mm in length and 80 mm in width. The distance between the fuel and air inlets is 165 mm, referred to as the inlet spacing in subsequent analyses. To achieve staged combustion, a three-stage air supply system is incorporated in the ascending

flue, with the secondary and tertiary air inlets positioned at vertical heights of 1945 mm and 3795 mm, respectively.

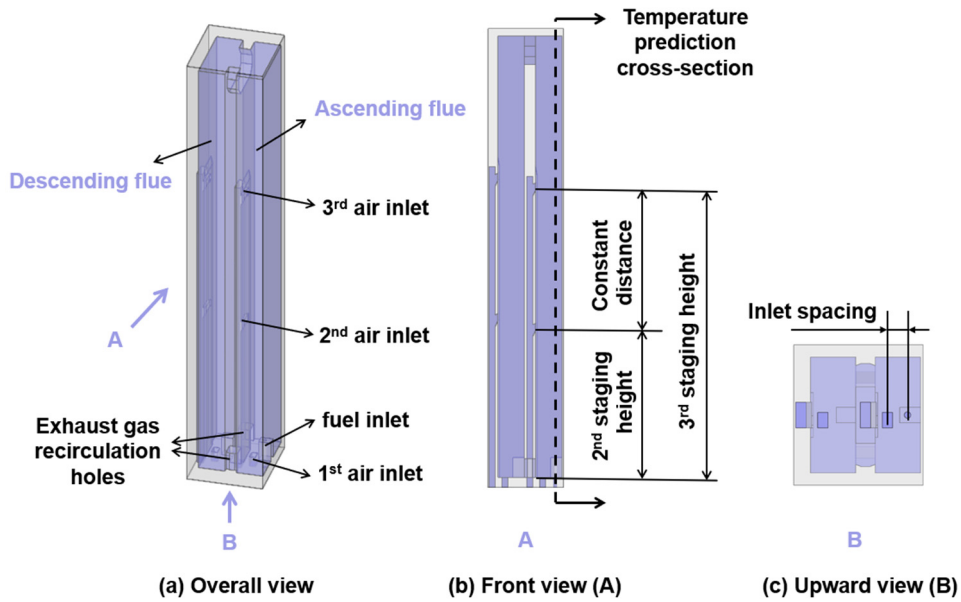


Figure 2. Geometry of the combustion chamber in the cook oven (**a**) overall view; (**b**) front view; (**c**) upward view.

Table 1. Structural parameters of the studied combustion chamber.

Variables	Values (mm)
Length of the flue	898
Width of the flue	350
Height of the flue	5811
Diameter of the fuel inlet	50
Length of the 1st air inlet	120
Width of the 1st air inlet	80
Height of the 2nd air inlet	1945
Height of the 3rd air inlet	3795
Thickness of the flue wall	150
Thickness of the cooking wall	95

2.2. Numerical Models

Due to the limited availability of experimental measurements, numerical simulation was conducted to reproduce temperature distributions and NO_x emissions under different combustion chamber structures, providing sufficient samples for ML model training. Based on the structure of the combustion chamber, a numerical model of a representative twin-flue unit within the combustion chamber is established in this study. The gas flow in the heating flues and combustion chamber is simulated using the transient Reynolds-Averaged Navier–Stokes (RANS) equations, and the gas mixture is treated as an incompressible ideal gas for computational simplicity. Due to the simple flow structure in the combustion chamber, the standard k-ε model and standard wall function are used in this study to accelerate convergence and improve numerical robustness according to the studies [4,10,31,32]. The fully developed flow is assumed to enhance computational stability and efficiency.

For combustion modeling, the species transport approach is adopted using the Eddy Dissipation Concept (EDC) model. The EDC framework assumes that chemical reactions occur within fine turbulent eddies, where reaction rates are determined by the competition between turbulent mixing timescales and chemical kinetic timescales. This approach

enables the coupled effects of turbulent mixing and chemical kinetics. The radiation heat transfer model employs the discrete ordinates (DO) model, whilst the gas absorption coefficient utilizes the weighted-sum-of-gray-gas (WSGG) model. This configuration effectively handles non-gray body radiation, rendering it highly suitable for describing heat transfer processes within coke oven combustion chambers [4]. The furnace gas composition used in this study contains seven species, including CH_4, C_2H_4, CO, CO_2, O_2, N_2, and H_2. It is assumed that all gases behave as ideal gases. Based on the GRI 3.0 chemical mechanism [33], a reduced chemical mechanism consisting of 26 species and 112 reactions is developed using the decoupling methodology [34].

The governing equations for continuity, momentum, energy, and species transport used in the CFD simulations are shown in Equations (1)–(4).

$$\frac{\partial \rho}{\partial t} + \nabla \cdot (\rho \boldsymbol{u}) = 0 \tag{1}$$

$$\frac{\partial (\rho \boldsymbol{u})}{\partial t} + \nabla \cdot (\rho \boldsymbol{u}\boldsymbol{u}) = \nabla \cdot (\mu_{\text{eff}} \nabla \boldsymbol{u}) - \nabla P + \boldsymbol{F_s} \tag{2}$$

$$\frac{\partial (\rho h)}{\partial t} + \nabla \cdot (\rho h \boldsymbol{u}) = \nabla \cdot \left(\lambda_{\text{eff}} \nabla T - \sum_j h_j \boldsymbol{J}_j \right) + S_h \tag{3}$$

$$\frac{\partial (\rho Y_j)}{\partial t} + \nabla \cdot (\rho \boldsymbol{u} Y_j) = -\nabla \cdot \boldsymbol{J}_j + \omega_j \tag{4}$$

where ρ is fluid density; t is time; $\boldsymbol{u}$ is fluid velocity; μ_{eff} is effective dynamic viscosity, P is pressure; $\boldsymbol{F_s}$ is volume force; h is the specific total enthalpy of the mixture; λ_{eff} is effective thermal conductivity; h_j is specific enthalpy of species j; $\boldsymbol{J}_j$ is diffusion flux of species j; S_h is the heat generation rate from chemical reactions; Y_j is mass fraction of species j; and ω_j is the rate of formation of species j due to chemical reactions.

A block-structured hexahedral mesh is employed with local refinement in the inlet and outlet regions to accurately resolve high-gradient flow features. A grid sensitivity is performed, as shown in Figure 3. The results indicate that reducing the base mesh size from 3 to 2 cm leads to obvious variations in maximum combustion temperature and emissions. However, further refinement beyond 2 cm yields negligible improvements in the overall predicted results. Therefore, to balance computational efficiency and accuracy for the large computational domain, a base mesh size of 2 cm with cell numbers of 300,000 is finally selected for all the following simulations.

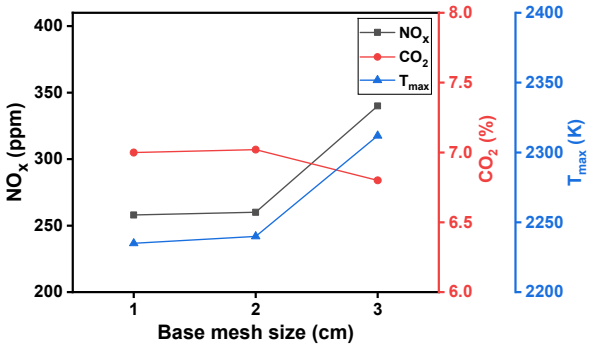


Figure 3. Grid independence verification results.

The inlet and outlet flow rates, temperatures, and boundary conditions are shown in Table 2. Gas fuel is only supplied at the bottom of the combustion chamber, which is defined as a mass flow inlet condition. Air is supplied through two channels, both of which are modeled as mass flow inlets with a total flow rate of 0.02674 kg/s. The primary air inlet is located at the bottom, and the remaining air is supplied via another channel for the

secondary and tertiary inlets. The air staging ratio refers to the flow ratio of the primary air inlet, which is regulated by coordinating the relative openings of the primary and secondary air dampers. The walls of the combustion chamber adjacent to the coking chamber are assigned a predefined temperature boundary condition, and the other walls are assumed as adiabatic boundaries. To accurately simulate the combustion process within the coke oven, an unsteady-state calculation approach is adopted. The convergence criterion is set to residuals below 0.001, with a minimum time step of 0.001 s to balance computational accuracy and efficiency. Due to the large computational domain and the complex chemical kinetics calculation, all CFD cases are solved using parallel processing on 64 CPU cores.

Table 2. Operating and boundary parameters of the combustion chamber.

Variables	Value
Gas flow rate	0.002076 kg/s
Gas temperature	873 K
Total air flow rate	0.02674 kg/s
Air temperature	1373 K
Outlet pressure	101,225 Pa
Wall temperature	1375 K
Excess air ratio	1.2

2.3. Neural Network Model

CNNs are particularly well-suited for characterizing spatial distributions owing to their inherent capability to model spatial hierarchies, effectively capturing critical local spatial correlations and multi-scale dependencies [35]. However, the structural parameters of the combustion chamber are adjusted in this paper, resulting in significant variations in spatial fields. To address the complex mapping problem from physical parameters to high-dimensional field distributions, a PFCN based on a heterogeneous dual-stream encoding–fusion–decoding architecture is proposed. The main architectural framework of the built model is illustrated in Figure 4.

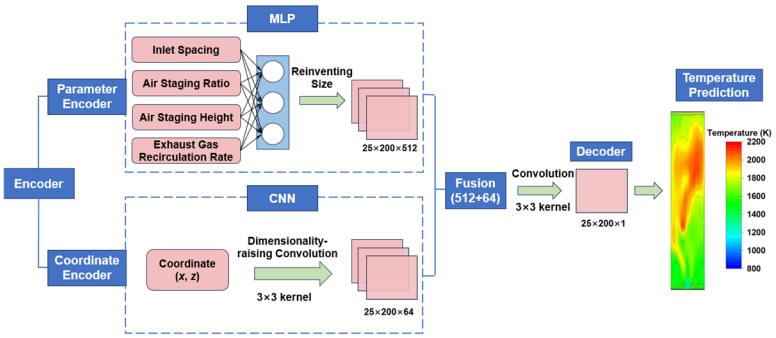


Figure 4. Schematic structure of the proposed PFCN.

To accommodate the different dimensional scales and magnitudes between structural parameters and spatial coordinates as model inputs, MLP and CNN are accordingly integrated as encoders to handle scalar parameters and spatial coordinates. Coupled with a strategically designed feature fusion and decoding strategy, this heterogeneous framework significantly improves the predictive accuracy and generalization ability for temperature field reconstruction under limited available data [36]. Key improvements and architectural details are elaborated in the following sections.

2.3.1. Heterogeneous Two-Stream Encoder for Feature Extraction

To mitigate interference between structural and coordinate features, two heterogeneous encoding pathways are employed. Leveraging its ability to directly process structured grid data through sliding operations, a CNN is employed to encode the planar coordinate parameters. Local structural features are extracted by a multi-scale convolution kernel to capture key structural information, such as spatial gradients. The convolutional computation is defined as follows:

$$\boldsymbol{F}_{\mathrm{c}} = f_{\mathrm{conv}}^{(2)} \circ f_{\mathrm{conv}}^{(1)}(\boldsymbol{C}), \boldsymbol{C} \in \boldsymbol{R}^{H \times W \times 2} \tag{5}$$

$$f_{\mathrm{conv}}(\boldsymbol{x}) = \sigma_{\mathrm{GELU}}(\mathrm{BatchNorm}(\mathrm{Conv2D}_{3\times3}(\boldsymbol{x}))) \tag{6}$$

$$\mathrm{BatchNorm}(x) = \gamma \odot \frac{x-\mu}{\sqrt{\sigma^2+\epsilon}} + \beta \tag{7}$$

where $\boldsymbol{C}$ is the spatial coordinate matrix; $f_{\mathrm{conv}}^{(1)}$ and $f_{\mathrm{conv}}^{(2)}$ are the convolution block; $\boldsymbol{F}_{\mathrm{c}}$ is the coordinate parameters feature tensor; Conv2D denotes two-dimensional convolution operation; BatchNorm represents the batch normalization; μ is the mean value; σ is the standard deviation; ϵ is the extremely small constant; and γ and β are the learnable parameters.

After batch normalization, the training data is conformed to a standard normal distribution. The Gaussian error linear unit (GELU) is chosen as the activation function for coordinate encoding due to its continuous differentiability over the entire input domain and its probabilistic grounding in the Gaussian distribution. Compared to the rectified linear unit (ReLU), the GELU function more accurately aligns with the spatially continuous and gradually varying characteristics of physical temperature distributions, due to its smoother gradients. Furthermore, the GELU helps mitigate the inherent noise amplification in activation functions, benefiting from its gradual saturation property [37]. It is defined as follows:

$$\sigma_{\mathrm{GELU}}(x) = x \cdot \Phi(x) = x \cdot \frac{1}{2}\left[1 + \mathrm{erf}\left(\frac{x}{\sqrt{2}}\right)\right] \tag{8}$$

where $\Phi(x)$ is the cumulative distribution function of the standard normal distribution, and erf is the Gaussian error function.

Unlike the spatial coordinate matrix, the structural parameters are represented as a feature vector. Accordingly, this study employs an MLP to encode these structural parameters, which are transformed into high-dimensional vectors through hierarchical nonlinear transformations [38]. In MLP, the LeakyReLU is adopted as the activation function due to its ability to alleviate the vanishing gradient problem and prevent neuron inactivity [39]. It is defined as:

$$f(x) = \begin{cases} x, & \text{if } x > 0 \\ a \cdot x, & \text{if } x < 0 \end{cases} \tag{9}$$

where a is the slope of the negative part in the coordinate system to prevent the gradient from disappearing.

The dual-stream encoder architecture addresses the inherent limitations of traditional monolithic encoder paradigms by decoupling the parametric and spatial features. This segregation encoding mitigates mutual interference between the heterogeneous feature types, thereby enabling a more precise identification of their complex nonlinear coupling relationships.

2.3.2. Feature Fusion Module for Cross-Modal Feature Integration

Following independent feature extraction in the dual-stream encoder, a tailored fusion strategy is employed to integrate the heterogeneous structural and coordinate features. To

address the intrinsic discrepancies in scale and dimensionality among different features, an interpolation–splicing–compression fusion framework is proposed in this study. Specifically, the structural parameter features undergo spatial upsampling via nearest-neighbor interpolation to achieve consistent spatial resolution parity with the coordinate features. Subsequently, the aligned feature tensors are concatenated along the channel dimension, which can integrate both the global contextual influence of the structural parameters and the spatially localized coordinate properties within a unified representation space. The process can be described as follows:

$$\boldsymbol{F}_{\mathrm{p}} = \mathrm{Interp}_{\mathrm{nearest}}\left(h_{\mathrm{p}}, (H, W)\right) \in R^{H \times W \times C} \tag{10}$$

$$\boldsymbol{F}_{\mathrm{cat}} = \boldsymbol{F_{\mathrm{p}}} \oplus \boldsymbol{F_{\mathrm{c}}} \in R^{H \times W \times C} \tag{11}$$

where $\boldsymbol{F}_{\mathrm{p}}$ is the extended structural parameters feature tensor; $\boldsymbol{F}_{\mathrm{cat}}$ is the vector after splicing; $\boldsymbol{F_{\mathrm{c}}}$ is defined in Equation (5) referring to the coordinate parameters feature tensor; h_{p} is the parameter feature tensor; H is the height of the tensor; W is the width of the tensor; C is the feature dimension; and $\mathrm{Interp}_{\mathrm{nearest}}$ is the nearest neighbor interpolation processing.

This hierarchical interpolation–splicing–compression strategy effectively reconciles the discrepancies in scale and dimensionality, enabling robust modeling of the complex nonlinear couplings. The fused feature tensor is then processed through a convolutional layer with nonlinear activation, generating hierarchical representations specifically tailored to capture the thermophysical patterns essential for temperature field reconstruction. Consequently, this fusion strategy not only enhances the adaptivity of the model to cross-modal interaction but also establishes a multi-scale feature foundation critical for the subsequent decoding stages.

2.3.3. Residual Block Enhanced Hierarchical Decoder for Stable Convergence

The decoder architecture employs a sequence of upsampling and refinement stages to progressively increase the spatial resolution of the feature maps while enhancing their representational fidelity. Through successive layers comprising transposed convolutions, batch normalization, and nonlinear activation functions, the network learns to transform the fused feature representation into a full-resolution temperature field distribution that maintains strict spatial registration with the input coordinate system. This hierarchical decoding process effectively reverses the feature extraction procedure, ultimately yielding a high-fidelity reconstruction of the temperature field. Meanwhile, to enhance the feature representation capability and mitigate the gradient vanishing problem, a residual block mechanism is introduced [40]:

$$\mathcal{F}(\boldsymbol{x}) = \mathrm{BN}(\boldsymbol{W_2} \cdot \sigma_{\mathrm{GELU}}(\mathrm{BN}(\boldsymbol{W_1 x}))) \tag{12}$$

$$\boldsymbol{y} = \mathcal{F}(\boldsymbol{x}) + \boldsymbol{x} \tag{13}$$

where $\boldsymbol{W_1}$ and $\boldsymbol{W_2}$ are 3×3 convolution weights; BN is batch normalization; and $\boldsymbol{y}$ is the output of residual block. This structure allows the input to skip multiple layers and to be added directly to the output, facilitating more direct gradient propagation to previous layers. This mechanism helps alleviate the gradient vanishing problem during backpropagation and optimize the network easier.

Finally, the decoding process culminates in a pointwise convolutional layer that projects the high-dimensional feature representation onto the target temperature field, as shown in Equation (14). This design ensures spatial consistency between the output prediction and the input coordinate grid resolution. Critically, the entire decoder architecture is specifically engineered to invert the feature abstraction process, transforming

the learned high-level representations back into concrete physical field distributions. This methodology inherently incorporates prior knowledge regarding the reduction from abstract features to physical observables, enhancing the predictive accuracy and ensuring physically plausible results.

$$\boldsymbol{T}_{\text{pred}} = \boldsymbol{W}_{\mathbf{out}} \times \boldsymbol{F}_{\text{dec}},\ \boldsymbol{W}_{\mathbf{out}} \in R^{1\times1\times256\times1} \tag{14}$$

where $\boldsymbol{T}_{\text{pred}}$ is the predicted temperature field, $\boldsymbol{W}_{\mathbf{out}}$ is the 1×1 convolutional kernel weight matrix that maps the high-dimensional features to a single-channel output, and $\boldsymbol{F}_{\text{dec}}$ is the high-level feature output from the decoder.

In summary, the proposed model employs dedicated parameter and coordinate encoders to perform independent feature extraction for distinct types of inputs. These features are then organically integrated within the fusion module, enabling the decoder to accurately reconstruct the target temperature field from the fused latent representation. This hierarchical processing pipeline not only enhances the feature learning capacity of the model but also improves the adaptability and robustness of the model for predicting complex physical fields.

2.4. Support Vector Machine for NO_x Predictions

Different combustion chamber structures affect the combustion temperature, leading to varying levels of NO_x emissions. SVM is a classical supervised learning algorithm, primarily employed for classification and regression tasks with high generalization capability [41]. Therefore, SVM is employed to establish the nonlinear correlation between structural parameters and NO_x emissions. Since the NO_x formation in the coke oven combustion chamber is primarily thermally induced and directly correlated with combustion temperatures [3], the temperature statistics derived from PFCN predictions are also incorporated as physics-informed inputs for NO_x prediction. As illustrated in Figure 5, the highest and lowest combustion temperatures are integrated with these structural parameters of inlet spacing, air staging ratio, air staging height, and exhaust gas circulation rate as inputs to train the SVM model for NO_x emissions prediction [42].

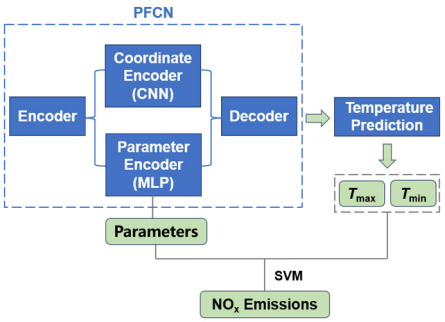


Figure 5. Flowchart of NO_x predictions using SVM based on the temperature predictions from PFCN.

2.5. Training Process of PFCN for Temperature Predictions and SVM for NO_x Predictions

The training dataset is derived from the CFD simulations of coke oven combustion chambers under five different combinations of structural parameters, including inlet spacing, air staging ratio, air staging height, and exhaust gas recirculation rate. The vertical section for predicted temperature distribution is taken through the gas inlet in the ascending flue, which can accurately reflect the temperature distribution in the whole combustion chamber under different conditions, as seen in Figure 2. To preserve the spatial integrity essential for convolutional operations, samples are partitioned exclusively by their structural parameters. This partitioning strategy ensures that both the training and validation

sets contain complete spatial information (i.e., the full coordinate grid and temperature field) for each unique structural configuration, maintaining topological coherence within individual samples. The dimensions and processing methods of the dataset are shown in Table 3. The dataset comprises 65 samples, each characterized by five structural parameters and a corresponding 25 × 200 cross-sectional temperature field. The data are split into training and validation sets in an 80:20 ratio.

Table 3. Dimensions and processing methods of the dataset.

Variables	Values
Input tensor dimensions of PFCN (H × W × C)	25 × 200 × 5
Tensor dimensions after fusion (H × W × C)	25 × 200 × (512 + 64)
Output tensor dimensions of PFCN (H × W × C)	25 × 200 × 1
Size of dataset	65
Proportions of training and validation sets	80:20
Data normalization methods	Z-Score Normalization

The Adam optimizer inherently couples the weight decay factor to the learning rate schedule, rendering the effective regularization strength dependent on the learning rate magnitude. On the contrary, the AdamW optimizer decouples weight decay from gradient computation by applying regularization directly to weights [43], thereby mitigating the detrimental interference from adaptive learning rates and enhancing generalization capacity [44]. This decoupling proves particularly advantageous for temperature field prediction, which necessitates processing inherently heterogeneous structural parameters and spatial coordinates. Thus, AdamW is adopted in this study, where weight decay is implemented by direct gradient modification instead, as demonstrated as follows:

$$\theta_t \leftarrow \theta_{t-1} - \eta\left(\frac{m_t}{\sqrt{v_t}+\epsilon} + \lambda\theta_{t-1}\right) \tag{15}$$

where λ is the weight decay coefficient, η is the learning rate, θ_t is the model parameter (weight) at time t, and m_t and v_t are the bias correction value for the moment estimated at time t.

The adaptive learning rates of AdamW dynamically balance update magnitudes across distinct feature types, achieving accelerated convergence and enhanced stability in high-dimensional physical field regression. The AdamW optimizer with an initial learning rate of 0.001 is used to balance convergence speed and training stability. The learning rate is then dynamically updated based on the validation loss; if the validation loss does not decrease significantly for 20 consecutive epochs, the learning rate is automatically reduced to improve the convergence performance. L2 regularization (with a weight decay coefficient of 1.0×10^{-5}) is incorporated to control the network complexity and mitigate overfitting [45]. To further prevent overfitting, early stopping is also incorporated. Figure 6 depicts the convergence behavior of training and validation losses throughout the PFCN optimization process. It can be seen that both metrics descend to thresholds aligning with theoretical expectations, indicating the effective model optimization.

The SVM model undergoes five-fold cross-validation, and the model exhibiting the minimal root mean square error (MSE) is selected as the optimal model for the subsequent prediction and optimization. The MSE curve obtained from the training process is shown in Figure 7. The observed minimum MSE refers to the smallest MSE calculated through cross-validation across all attempted parameter combinations, and the estimated minimum MSE represents the globally optimal value predicted by the model. It can be seen that the two curves are nearly superimposed, and the MSE decreases steadily to a certain level

without further improvements, which indicates that the model has achieved its optimal convergence state.

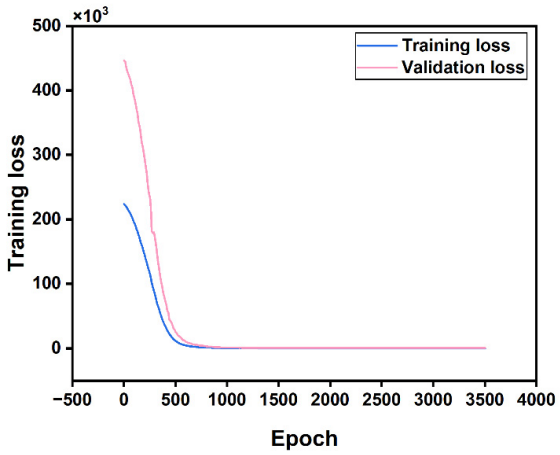


Figure 6. Loss curve during PFCN training.

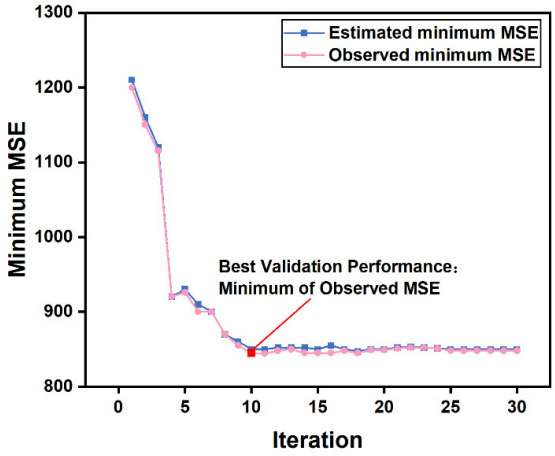


Figure 7. Mean square error curve of SVM models.

3. Model Validations

3.1. Validations of CFD Model

Given the challenges of in situ temperature measurements in industrial-scale coke ovens, the predictions of the main species concentrations are compared against the limited measured data from the combustion chamber with a three-stage air supply configuration described above [46]. As shown in Figure 8a, the calculated outlet emissions show good agreement with the experimental data, and the maximum component concentration error is less than 10%. Furthermore, the combustion chamber of a coke oven with a similar structural size and single-stage air supply is simulated under the test operating conditions [47]. The vertical temperatures at four distinct heights within the ascending and descending flues were measured using thermocouples. As quantitatively compared in Figure 8b, the simulations show good agreement with the experimental measurements, with the calculation error below 5%. The above validation results confirm the reliability of the adopted numerical models, which will be used to accumulate data for PFCN model training.

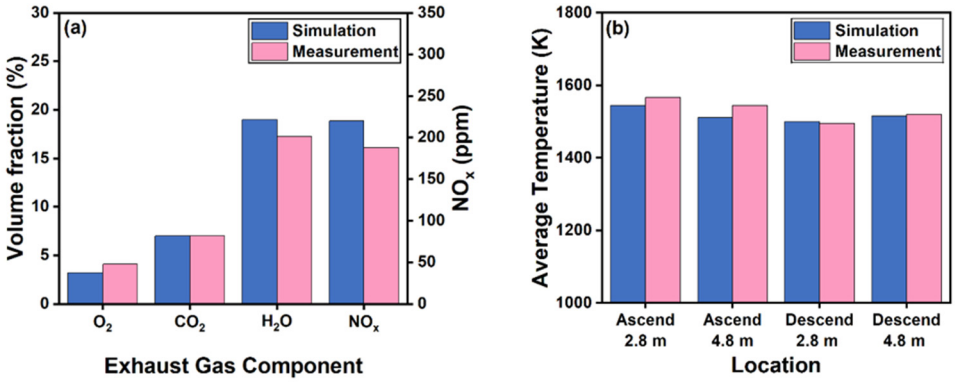


Figure 8. Comparison between simulation and experiment (**a**) the exhaust gas compositions; (**b**) the average temperatures at ascending and descending flues [46,47].

3.2. Validations of ML MODELS

Quantitative validation of the predicted temperature distribution is conducted through systematic comparison between CFD simulations and PFCN predictions in the combustion chamber of the test coke oven. To demonstrate the stability of the PFCN model, three representative cases with distinct structural parameters were selected from validation dataset for comparison. They are, respectively, named Cases 1~3, and their parameters are summarized in Table 4. As shown in Figure 9, the built PFCN model accurately predicts both the thermal gradient distribution and local high-temperature regions in different cases, with an average absolute deviation below 5% for spatial temperature distribution.

Table 4. Structural parameters of test samples.

Variables	Case 1	Case 2	Case 3
Inlet spacing (mm)	145	175	165
Air staging ratio (−)	0.4	0.5	0.45
Second air staging height (mm)	1549	1549	1945
Third air staging height (mm)	3399	3795	3399
Exhaust gas recirculation rate (−)	0.238	0.238	0.238

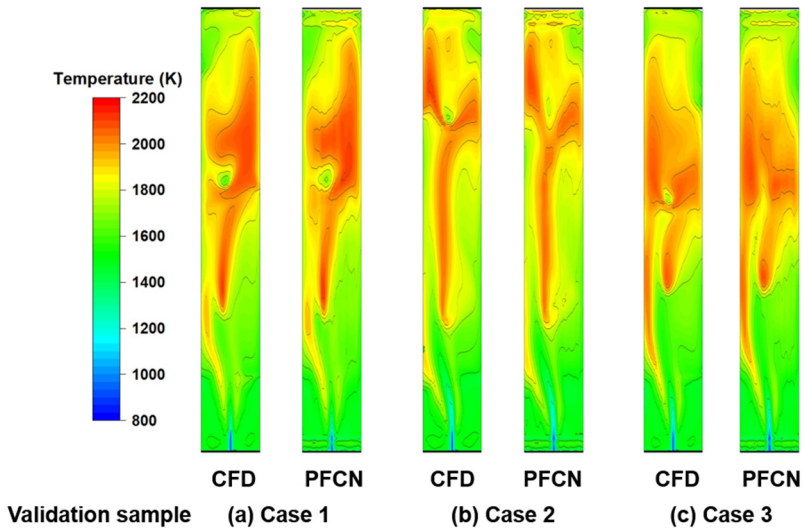


Figure 9. Comparison of the predicted temperature distributions between PFCN and CFD for (**a**) Case 1; (**b**) Case 2; (**c**) Case 3.

For the five optimized parameters, i.e., inlet spacing, air staging ratio, the second air inlet height, the third air inlet height, and flue gas recirculation rate, a total of 65 cases are designed using Sobol sampling for the training of both the PFCN and the SVM models. The variation ranges of the five parameters are listed in Table 5, and the basecase is the original design structure of the validated combustion chamber. To quantify the uniformity of the vertical temperature distribution inside the heating flue, the inhomogeneity of temperature is characterized by the standard deviation of temperature (β) in the chosen cross-section, and the definition of β is as follows:

$$\beta = \sqrt{\frac{1}{n}\sum_{i=1}^{n}(y_i - T_a)^2} \tag{16}$$

where n is the number of points on the extracted plane, y_i is the temperature of each extracted point, T_a is the average temperature of all points, and β is the standard deviation of temperature.

Table 5. Variation range of the structural parameters.

Variables	Basecase	Range
Inlet spacing (mm)	165	145–165
Air staging ratio (−)	0.5	0.4–0.6
Second air staging height (mm)	1945	±396
Third air staging height (mm)	3795	±396
Exhaust gas recirculation rate (−)	0.253	0.238–0.269

As shown in Figure 10, the PFCN model demonstrates high fidelity in predicting the thermal gradient distribution across all the test cases, with the average absolute deviation within 5%. Concurrently, the SVM-based NO_x emission predictions remain in close agreement with the CFD simulation. Quantitative evaluation shows that the coefficient of determination (R^2) reaches 0.95 for inhomogeneity of temperature and 0.8 for NO_x emissions, which can be considered acceptable for engineering applications. The quantitative agreement between the CFD simulation and the ML predictions demonstrates the reliability of the developed the PFCN and SVM models in accurately capturing the working process in the combustion chamber, which will be applied to subsequent exploration and optimization. Further validation results can also be found in the subsequent Section 4.

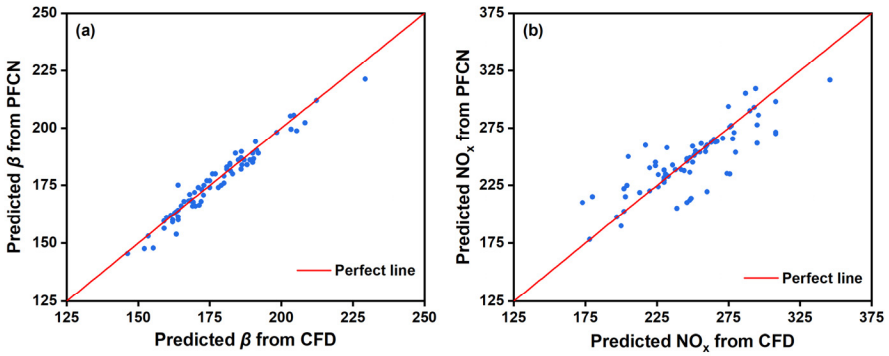


Figure 10. Comparison between CFD and PFCN (**a**) temperature inhomogeneity (β); (**b**) NO_x.

Furthermore, an ablation experiment is conducted to evaluate the effectiveness of the proposed interpolation–splicing–compression framework. Accordingly, a single convolution module (i.e., CNN) is introduced by removing the dual-stream encoder and fusion module in PFCN model. For Case 1, despite the CNN model using the same configuration

as PFCN, it not only overpredicts the overall temperature value, but also fails to accurately capture the local low-temperature combustion region, as seen in Figure 11. Meanwhile, when the PFCN is replaced by the CNN model, MSE of temperature increases from 180 to 1543. All these results demonstrate the superiority of the PFCN architecture in predicting the temperature field.

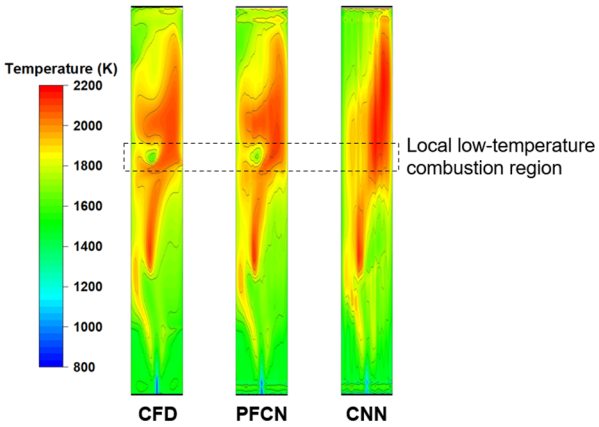


Figure 11. Comparison of temperature contour maps among CFD, PFCN, and CNN for Case 1.

4. Results and Discussion

A comparative analysis is conducted between CFD simulations and neural network predictions with respect to the five structural parameters, and the influences of these structural parameters on combustion temperature and NO_x emissions are investigated in detail in this section. Finally, the five structural parameters are optimized to achieve better performance.

4.1. Effect of Inlet Spacing

The effects of the inlet spacing between the air inlet and coke oven gas inlet at the bottom of the combustion chamber on the combustion and emissions are first explored. The inlet spacing see Figure 2 is varies from 145 to 185 mm with an increment of 20 mm. Comparisons of the cross-sectional temperature distributions under three different inlet spacings between CFD calculations and PFCN predictions are shown in Figure 12. Since the intake air is supplied through three discrete inlet holes corresponding to the three-stage air supply, the combustion in the ascending flue can be accordingly divided into three regions, as illustrated in Figure 12. All the combustion fields can be quantitatively captured by the PFCN model, especially the complex temperature distributions after the third air inlet hole in the third region. The relative error of PFCN predictions in cross-sectional temperature is less than 4%.

The statistical results of β and NO_x emissions under different inlet spacings are shown in Figure 13. It is found that a longer inlet spacing leads to a larger β and lower NO_x emissions. When the inlet spacing is increased, the contact interface area between the primary air and coke oven gas injected at the bottom decreases. This prolongs the time required for fuel/air mixing and combustion, and the high-temperature flame occurs at the further downstream location with a larger lift-off height. Furthermore, a longer fuel/air mixing duration also leaves more time for recirculated exhaust gas dilution, which also has negative effects on ignition and combustion. Thus, the location of the high-temperature flame is higher, and the peak combustion temperature is reduced with a larger inlet spacing. As a result, the temperature gradient along the vertical direction becomes smaller, resulting in an 11% reduction in temperature inhomogeneity, as seen in Figure 13.

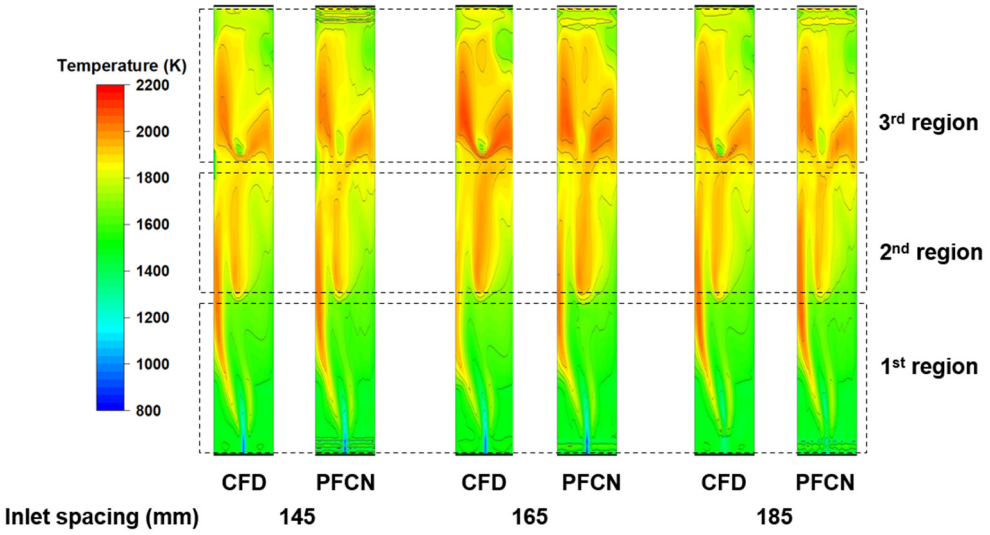


Figure 12. Comparison of the predicted temperature distributions between CFD and PFCN with different inlet spacings.

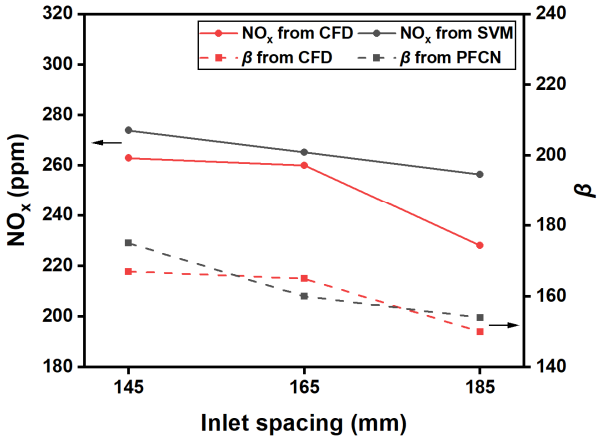


Figure 13. Variations in β and NO_X from both CFD and PFCN/SVM predictions under different inlet spacings.

NO_X emissions in the combustion chamber are mainly generated from thermal NO_X, which is very sensitive to high-temperature regions. Based on the precise prediction of the temperature inside the combustion chamber, the variation of NO_X emissions with the increase in inlet spacing is also accurately predicted by the developed SVM model. When the inlet spacing is increased from 145 to 165 mm, the maximum combustion temperature is reduced, and the NO_X emissions at the outlet are decreased by 13% accordingly, as observed in Figure 13.

4.2. Effect of Air Staging Ratio

When the total flow rate of inlet air is kept constant, the air staging ratio, i.e., the air ratio of the first stage air inlet hole at the bottom of the combustion chamber, is adjusted from 0.4 to 0.6, and the variations in flame structure and NO_X emissions are compared between CFD simulations and PFCN/SVM predictions, as shown in Figures 14 and 15.

As shown in Figure 14, both CFD simulations and PFCN predictions demonstrate that increasing the air staging ratio enhances combustion intensity in the first and second stages of the combustion zone, thereby elevating the combustion temperature in these regions. On the contrary, this oxygen left for the third combustion zone is insufficient, resulting in the deteriorated combustion [48]. When the air staging ratio is increased to 0.6, most

areas in the top region corresponding to the third zone of the ascending flue remain at a relatively low temperature, and more obvious temperature inhomogeneity can be observed, as illustrated in Figure 14. Both CFD and PFCN consistently reveal that β increases over 23% when the air staging ratio is increased from 0.4 to 0.6, as depicted in Figure 15.

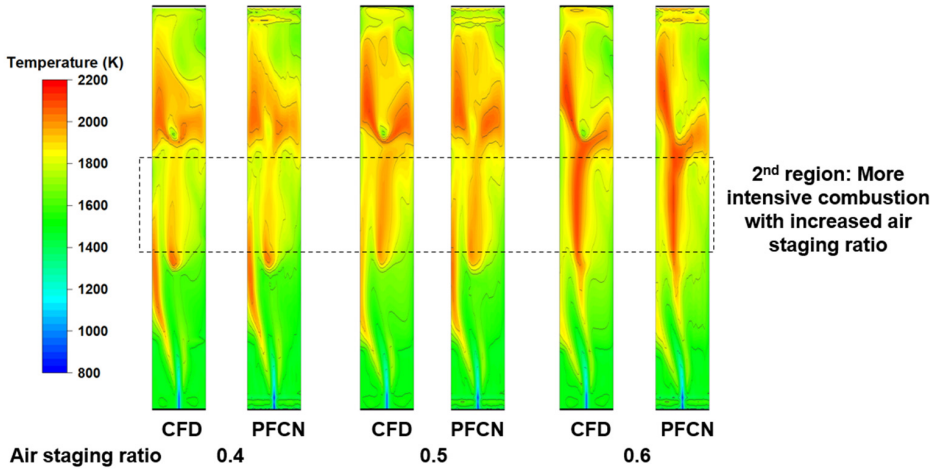


Figure 14. Comparison of the predicted temperature distributions between CNN and PFCN with different air staging ratios.

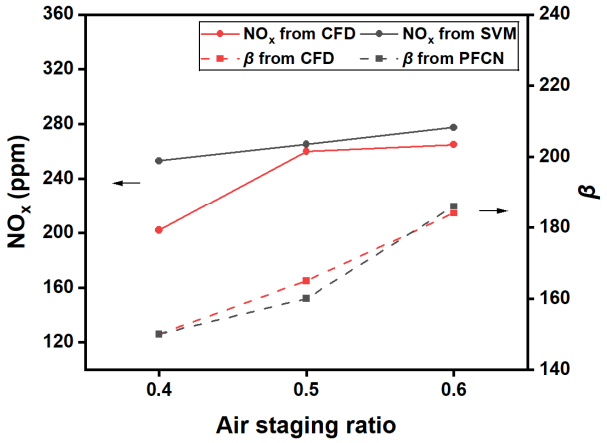


Figure 15. Variations in β and NOx emissions from both CFD and PFCN/SVM predictions under different air staging ratios.

When the air staging ratio is increased, the most intensive combustion region is shifted from the third stage zone to the second stage zone. Excessive oxygen intensifies local combustion due to the near-stoichiometric combustion, elevating the peak combustion temperature and promoting thermal NO_x formation. Thus, Figure 15 reveals that NO_x emissions are increased with the increased air staging ratio, and both CFD simulations and SVM predictions capture the consistent variation of NO_x.

4.3. Effect of Air Staging Height

The air staging height refers to the height of the third air inlet. Since the distance between the second and third air inlets is kept constant, adjusting the height of the third air inlet will accordingly change the height of the second air inlet (see Figure 2). Therefore, the heights of the two air inlets are adjusted simultaneously to investigate their effects on combustion and emissions. Based on the original structure of the combustion chamber, the air staging height is adjusted upward and downward by 396 mm, which corresponds to the height of three bricks used in the experimental construction. Both the PFCN model

for temperature field prediction and the SVM model for NO_x prediction demonstrate excellent agreement with the CFD simulation results, as observed in Figures 16 and 17. The maximum relative error of β and NO_x between the predicted and CFD results is kept below 10%.

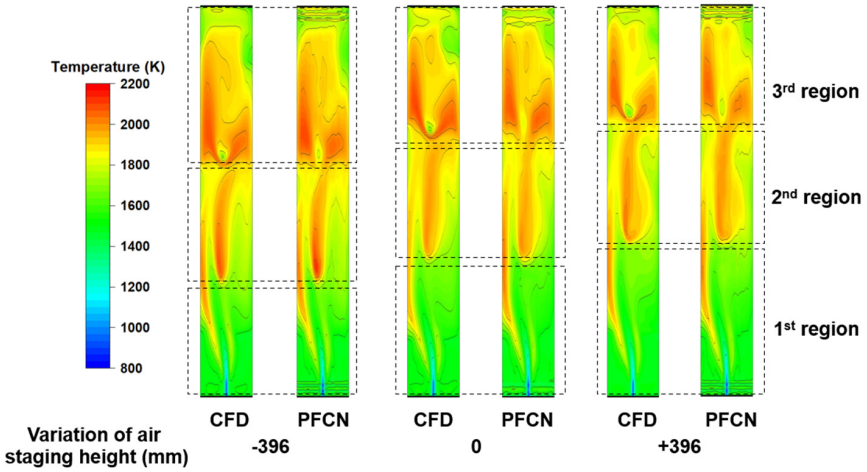


Figure 16. Comparison of the predicted temperature distributions between CFD and PFCN with different air staging heights.

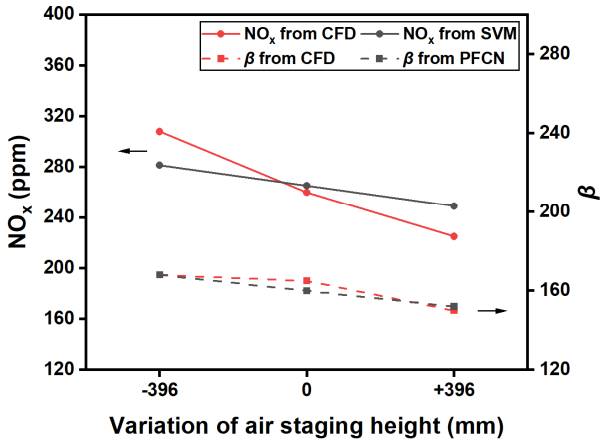


Figure 17. Variations in β and NO_x emissions from both CFD and PFCN/SVM predictions under different air staging heights.

As shown in Figure 16, the air staging height directly determines the vertical positions of the second and third combustion zones. When the air staging height is reduced, the distance between the first stage combustion and the second stage combustion zones becomes smaller, leaving insufficient space and time for the first stage combustion. Thus, the incompletely oxidized products from the first stage will be further oxidized in the subsequent combustion stages, resulting in the higher combustion temperatures in the second and third stages. As a result, the temperature difference along the vertical direction of the combustion chamber becomes larger. On the contrary, with the increase in air staging height, the more complete combustion in the first stage causes a higher local combustion temperature, and the combustion intensities of the second and third stages are reduced accordingly, contributing to the reduction in β.

When the air staging height is reduced, the more intensive combustion in the second and third stages leads to higher NO_x emissions. The increased air staging height also causes the positions of the second and third stage combustion to move farther from the first stage combustion. Meanwhile, the space left for the third stage combustion becomes shorter,

which is unfavorable to the third stage combustion. Therefore, with a larger air staging height, the overall combustion temperature is reduced, and the NO_x emissions are reduced, as seen in Figure 17.

4.4. Effect of Exhaust Gas Recirculation

The ascending and descending flues in the combustion chamber are separated by vertically arranged silica brick partition walls. Two exhaust gas recirculation (EGR) holes are located near the bottom of the combustion chamber, which are used to reintroduce the combustion products (primarily CO_2 and H_2O) from the descending flue into the ascending flue. This can control combustion temperature and suppress NO_x formation. Since the recirculated exhaust gas flow is very difficult to measure accurately in the experiment, the EGR rate is usually defined based on the surface area of the exhaust gas recirculation hole as follows:

$$\text{EGR Rate} = \frac{S_{\text{recirculation hole}}}{S_{\text{heating flue}}} \tag{17}$$

where $S_{\text{recirculation hole}}$ is the cross-sectional area of the exhaust gas recirculation holes, and $S_{\text{heating flue}}$ is the cross-sectional area of a single heating flue.

The size of EGR holes is adjusted to change the EGR rate from 0.238 to 0.269, and the effect of EGR on both β and NO_x emissions is comprehensively investigated. As shown in Figures 18 and 19, the temperature distribution predicted by the PFCN and the CFD calculation results are consistent with the largest deviation of 8%, and the variation of NO_x emissions with the change in EGR rate is also well reproduced by the SVM model. The results demonstrate that higher EGR rates significantly lower the combustion temperature and reduce NO_x formation [14], which can be attributed to three reasons: thermal, dilution, and chemical effects. The high specific heat capacity of exhaust gas components (primarily CO_2 and H_2O) slows down the rise in combustion temperature and weakens combustion intensity. The introduced exhaust gas also dilutes the intake air and reduces the excess air ratio of the fuel/air mixture, thereby slowing the combustion rate. In addition, the CO_2 and H_2O introduced with the exhaust gas perform a chemical inertial effect, which contributes to a slower combustion rate and a lower combustion temperature. Therefore, NO_x emissions are reduced with a larger EGR rate. The lower peak combustion temperature with a larger EGR rate, especially in the third stage zone, reduces the temperature gradient in the chamber, resulting in better temperature uniformity and lower NO_x emissions.

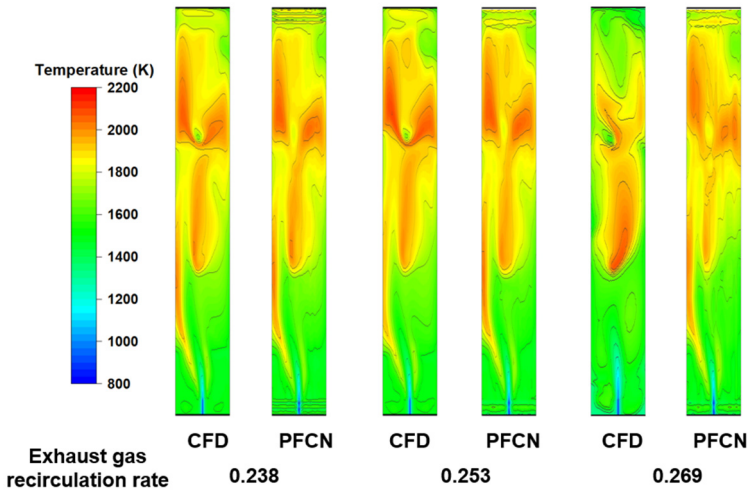


Figure 18. Comparison of the predicted temperature distribution between PFCN and CFD with different exhaust gas recirculation rates.

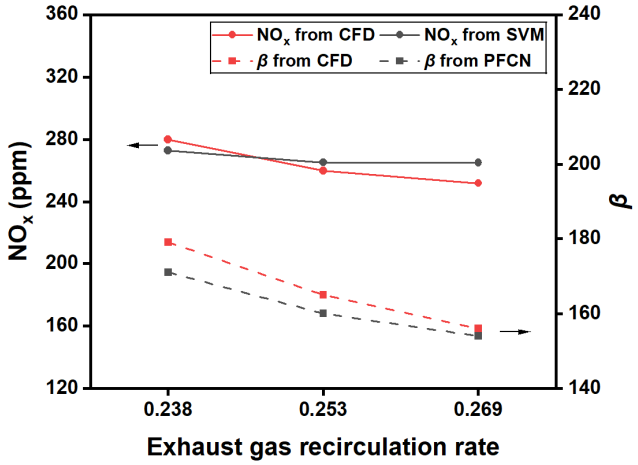


Figure 19. Variations in β and NO_x emissions from both CFD and PFCN/SVM predictions under various exhaust gas recirculation rates.

4.5. Parameter Sensitivity Analysis

Through the above comprehensive investigation of the influencing factors, the sensitivity analysis of each structural parameter on β and NO_x emissions is conducted in this section using the random forest (RF) method. To ensure robust prediction performance, the RF model is configured with 161 trees, each constrained to a maximum depth of 37. The minimum number of samples required for leaf nodes is two to prevent overfitting. Feature importance is evaluated using the mean dispersion of the impurities (MDI) method, which quantifies feature importance based on the probability-weighted sum of each feature's contribution to reaching internal nodes within the decision tree. The model is assessed via a five-fold cross-validation, yielding an optimal R^2 of 0.84 on the validation set. As shown in Figure 20, the air staging ratio shows the most significant influence on β, followed by the air staging height and EGR rate, and inlet spacing shows the least impact. With respect to NO_x emissions, the third air staging height and the air staging ratio exert the most significant effects. The evident effects of the air staging ratio stem from its direct control over the local excess air ratio and combustion intensity across all three combustion zones. The obvious influences of staging height derive from its impacts on adjusting the positions of the second and third high-temperature regions. These sensitivity analysis results are consistent with the experimental results [8,49], so they should be designed deliberately with higher priority.

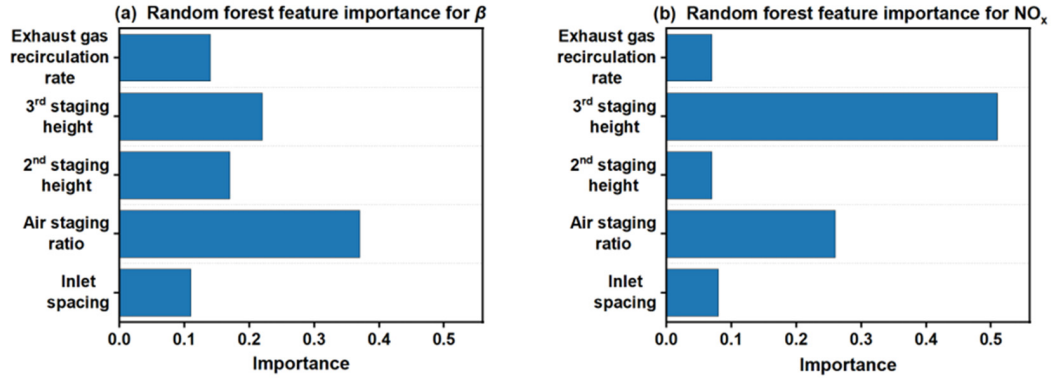


Figure 20. Sensitivity analysis of five structural parameters to (**a**) temperature inhomogeneity (β); (**b**) NO_x emissions.

4.6. Co-Optimization and Validation of Multiple Structural Parameters

Although the single-factor influences of each structural parameter of the combustion chamber have been investigated in the above discussions, the combined effects of multiple parameters must be considered together to further improve both the uniformity of combustion temperature and NO_x emissions in practical applications. Therefore, the co-optimization of the five key structural parameters (inlet spacing, air staging ratio, second and third air staging heights, and exhaust gas recirculation rate) is conducted by coupling the developed PFCN and SVM models with the genetic algorithm [50]. The performance evolution of the populations during the combustion process is shown in Figure 21, and the basecase is also added for comparison. From co-optimization, the optimal scheme achieves simultaneously low β and NO_x emissions without compromising the maximum temperature.

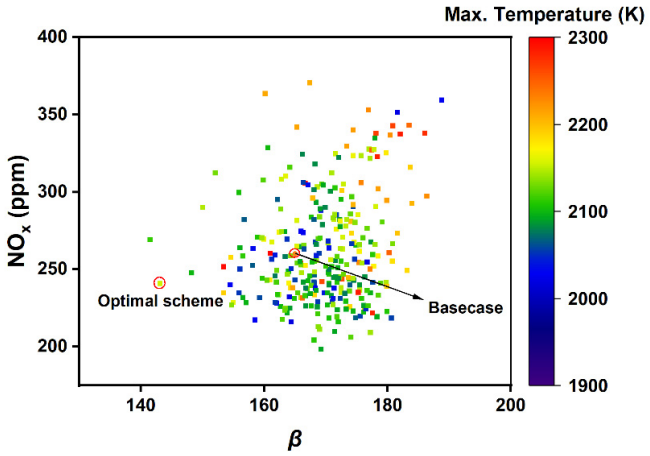


Figure 21. Comparison of performance between optimal scheme and basecase.

Furthermore, the reliability of the optimal scheme is verified by comparing the temperature distributions between the CFD simulation and the PFCN prediction, as shown in Figure 22a. The temperature distribution predicted by PFCN is highly consistent with that from the CFD calculation, and the improvements in both β and NO_x emissions are also accurately reproduced by the PFCN and SVM models with deviations below 5%, as shown in Figure 22b,c.

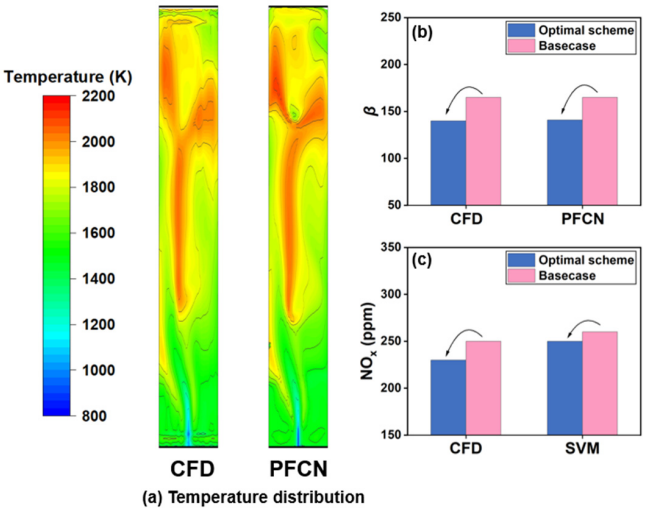


Figure 22. Comparison between CFD simulation and PFCN/SVM prediction for (**a**) temperature distribution; (**b**) temperature inhomogeneity (β); (**c**) NO_x emissions.

5. Conclusions

In order to accelerate the design process of the combustion chamber in coke ovens, the dual-stream PFCN and SVM models are proposed in this study to achieve real-time predictions of temperature distribution and combustion performance. The PFCN model is developed through independently processing structural parameters and spatial coordinates, optimizing activation functions, network topology, and learning rates, which shows high reliability in reconstructing the spatial temperature distributions in the combustion chamber under different conditions, with the largest deviation below 10%. Based on the temperature distribution predicted by PFCN, a SVM model is consequently built to predict NO_x emissions accurately.

According to the developed PFCN and SVM models, the effects of key parameters on combustion and emissions are immediately captured and visually presented. It is found that an increase in inlet spacing can promote the mixing of fuel and air, thereby enhancing the temperature uniformity in the vertical direction of the combustion chamber and reducing NO_x emissions. The reduction in air staging ratio can change the local combustion intensity, which is beneficial to improve both temperature uniformity and NO_x emissions. Increasing the air staging height directly elevates the spatial heights of the second and third combustion regions, yielding advantages for both temperature uniformity and NO_x emission reduction. A higher EGR rate can effectively reduce the combustion temperature and suppress NO_x formation.

Leveraging the high-fidelity predictive capabilities of the above-mentioned PFCN and SVM coupling framework, five critical structural parameters of the combustion chamber are co-optimized to further enhance temperature uniformity and NO_x emissions. The developed PFCN and SVM models are capable of instantly providing enhanced physical insights and more information compared with conventional CFD simulations, achieving 15.2% improvement in temperature homogeneity and 8% reduction in NOx emissions. Furthermore, the framework significantly accelerates the optimization design of industrial-scale coke ovens, which can also be used for transient process prediction, multi-system coupling analysis, and online control implementation.

However, there are still several aspects that merit further investigation to enhance its practical utility. First, the prediction accuracy of the current models can be further improved by incorporating attention mechanisms, physical constraints, etc. Second, the model output could be expanded to more performance indicators, such as species concentrations, thermal efficiency, etc., enabling a more comprehensive assessment of combustion performance under varying conditions. Finally, for the online control applications, the real-time sensor data should be introduced as dynamic inputs to the network, allowing closed loop adjustment of operating parameters based on actual combustion states.

Author Contributions: Conceptualization, Y.S.; Methodology, X.N.; Software, X.N.; Validation, C.Y.; Formal analysis, C.Y. and Y.L.; Investigation, Y.S. and C.Y.; Resources, M.W.; Writing—original draft, Y.S. and C.Y.; Writing–review & editing, Y.L., M.J. and H.L.; Supervision, M.W., M.J. and H.L.; Project administration, Y.L.; Funding acquisition, M.J. All authors have read and agreed to the published version of the manuscript.

Funding: The work is financially supported by the National Natural Science Foundation of China (Grant Nos. 52406125 and 52325603), the Liaoning Province Key Research and Development "Unveiling and Commanding" Project (Grant No. 2023JH1/10400087), and the Dalian Key Research and Development "Unveiling and Commanding" Project (Grant No. 2023JB11GX005).

Data Availability Statement: The data presented in this study are available on request from the corresponding author due to sensitive information protection.

Conflicts of Interest: Authors Yuan Shan and Mingdeng Wang were employed by the company ACRE Coking & Refractory Engineering Consulting Corporation (Dalian), MCC. The remaining authors declare that the research was conducted in the absence of any commercial or financial relationships that could be construed as a potential conflict of interest.

Abbreviations

The following abbreviations are used in this manuscript:

CFD	Computational fluid dynamics
CNN	Convolutional neural network
GELU	Gaussian error linear unit
MILD	Moderate and intense low-oxygen dilution
ML	Machine learning
MLP	Multilayer perceptron
PFCN	Parameter fusion convolutional network
R^2	Coefficient of determination
RF	Random forest
SVM	Support vector machine

References

1. Farias Neto, G.W.; Leite, M.B.M.; Marcelino, T.O.A.C.; Carneiro, L.O.; Brito, K.D.; Brito, R.P. Optimizing the coke oven process by adjusting the temperature of the combustion chambers. *Energy* **2021**, *217*, 119419. [CrossRef]
2. Li, K.; Khanna, R.; Zhang, J.; Liu, Z.; Sahajwalla, V.; Yang, T.; Kong, D. The evolution of structural order, microstructure and mineral matter of metallurgical coke in a blast furnace: A review. *Fuel* **2014**, *133*, 194–215. [CrossRef]
3. Li, Z.; Yi, Q.; Zhang, Y.; Zhou, H.; Zhao, Y.; Huang, Y.; Gao, D.; Hao, Y. Numerical study and design strategy for a low emission coke oven system using oxy-fuel combustion of coke oven gas. *J. Clean. Prod.* **2020**, *252*, 119656. [CrossRef]
4. Buczyński, R.; Kim, R. On optimization of the coke oven twin-heating flue design providing a substantial reduction of NOx emissions part I: General description, validation of the models and interpretation of the results. *Fuel* **2022**, *323*, 124194. [CrossRef]
5. Sharma, S.; Pingulkar, H.; Chowdhury, A.; Kumar, S. A new emission reduction approach in MILD combustion through asymmetric fuel injection. *Combust. Flame* **2018**, *193*, 61–75. [CrossRef]
6. Bhatt, A.N.; Shrivastava, N. Application of artificial neural network for internal combustion engines: A state of the art review. *Arch. Comput. Methods Eng.* **2022**, *29*, 897–919. [CrossRef]
7. Le, X.; Zhang, Z.; Zha, X.; Mao, W.; Luo, C.; Li, X.; Wu, F.; Zhang, L. Effects of tertiary air injection on the reaction behavior and NOx emissions during pulverized coal air-staged MILD combustion. *Appl. Therm. Eng.* **2025**, *274*, 126799. [CrossRef]
8. Xu, Q.; Zou, Z.; Chen, Y.; Wang, K.; Du, Z.; Feng, J.; Ding, C.; Bai, Z.; Zang, Y.; Xiong, Y. Performance of a novel-type of heat flue in a coke oven based on high-temperature and low-oxygen diffusion combustion technology. *Fuel* **2020**, *267*, 117160. [CrossRef]
9. Lyu, Q.-G.; Zhu, S.-J.; Zhu, J.-G.; Wu, H.-X.; Fan, Y.-Q. Experimental study on NO emissions from pulverized char under MILD combustion in an O_2/CO_2 atmosphere preheated by a circulating fluidized bed. *Fuel Process. Technol.* **2018**, *176*, 43–49. [CrossRef]
10. Buczyński, R.; Kim, R. On optimization of the coke oven twin-heating flue design providing a substantial reduction of NO_x emissions. Part II: Optimized designs for COG- and MG- fired units as well as operating characteristics of the new heating flues. *Fuel* **2022**, *323*, 124193. [CrossRef]
11. Isaev, M.V.; Sultanguzin, I.A. Three-dimensional simulation of combustion processes in coke-battery furnace chambers. *Coke Chem.* **2010**, *53*, 305–310. [CrossRef]
12. Toapanta-Ramos, F.; Guashco Rubio, M.; Ortega-Loza, F.; Diaz, W. Numerical study of 3D heat transfer in heat sinks with circular profile fins using CFD. *Processes* **2025**, *13*, 3199. [CrossRef]
13. Yang, J.; Zhang, L.; Ji, G.; Li, J.; Liu, Z. The influence of the depth of tubing in downward-inclined horizontal wells for shale gas on the drainage and production effect. *Processes* **2025**, *13*, 3348. [CrossRef]
14. Gamrat, S.; Poraj, J.; Bodys, J.; Smolka, J.; Adamczyk, W. Influence of external flue gas recirculation on gas combustion in a coke oven heating system. *Fuel Process. Technol.* **2016**, *152*, 430–437. [CrossRef]
15. Yan, R.; Liu, Y.; Dai, C.; Wu, S.; Tian, H.; Li, Y.; Xiang, C.; Dang, L.; Wei, H. Numerical simulation and optimization of the multi-stage air/gas supply system in a coke oven battery with 7.1 m coking chambers. *Int. J. Coal Prep. Util.* **2025**, *45*, 368–389. [CrossRef]

16. Çıtmacı, B.; Luo, J.; Jang, J.B.; Canuso, V.; Richard, D.; Ren, Y.M.; Morales-Guio, C.G.; Christofides, P.D. Machine learning-based ethylene concentration estimation, real-time optimization and feedback control of an experimental electrochemical reactor. *Chem. Eng. Res. Des.* **2022**, *185*, 87–107. [CrossRef]
17. Cai, K.; Feng, K.; He, D.; Yang, L.; Zhang, M. Incorporation of control parameters into a kinetic model for decarburization during basic oxygen furnace (BOF) steelmaking. *Processes* **2025**, *13*, 3048. [CrossRef]
18. Dahiya, N.; Gupta, S.; Singh, S. A review paper on machine learning applications, advantages, and techniques. In Proceedings of the Electrochemical Society, Vancouver, BC, Canada, May 29–June 2 2022; IOP Science: Bristol, UK, 2022; Volume 107, p. 6137. [CrossRef]
19. Yan, X.; Cheng, H.; Chi, S.; Liu, S.; Zhu, Z. Spatiotemporal modeling of the total nitrogen concentration fields in a semi-enclosed water body using a TCN-LSTM-hybrid model. *Processes* **2025**, *13*, 3262. [CrossRef]
20. Brunton, S.L.; Noack, B.R.; Koumoutsakos, P. Machine learning for fluid mechanics. *Annu. Rev. Fluid Mech.* **2020**, *52*, 477–508. [CrossRef]
21. He, S.; Wang, M.; Zhang, J.; Tian, W.; Qiu, S.; Su, G.H. A deep-learning reduced-order model for thermal hydraulic characteristics rapid estimation of steam generators. *Int. J. Heat Mass Transf.* **2022**, *198*, 123424. [CrossRef]
22. Lei, Y.; Chen, Y.; Chen, J.; Liu, X.; Wu, X.; Chen, Y. A novel modeling strategy for the prediction on the concentration of H_2 and CH_4 in raw coke oven gas. *Energy* **2023**, *273*, 127126. [CrossRef]
23. Yang, B.; Liu, L.; Huang, H.; Wang, Y.; Li, D.; Yang, Q.; Yin, L.; Zhang, Z. A real-time temperature field prediction method for steel rolling heating furnaces based on graph neural networks. *Int. J. Heat Mass Transf.* **2024**, *235*, 126220. [CrossRef]
24. Xue, W.; Tang, Z.; Cao, S.; Lv, M.; Wang, Z.; Zhao, B.; Wang, G.; Lu, Y. Efficient online prediction and correction of 3D combustion temperature field in coal-fired boilers using GDNN. *Measurement* **2023**, *222*, 113507. [CrossRef]
25. Liu, H.-X.; Li, M.-J.; Guo, J.-Q.; Zhang, X.-K.; Hung, T.-C. Temperature prediction of submerged arc furnace in ironmaking industry based on residual spatial-temporal convolutional neural network. *Energy* **2024**, *309*, 133024. [CrossRef]
26. Yang, Y.; Zhang, J.; Chen, Z.X.; Guan, Y.; An, Q. Latent space-based machine learning prediction of coupled flame-flow fields in a hydrogen-enriched syngas combustor. *Int. J. Hydrogen Energy* **2024**, *95*, 650–665. [CrossRef]
27. Strässle, R.M.; Faldella, F.; Doll, U. Deep learning-based image segmentation for instantaneous flame front extraction. *Exp. Fluids* **2024**, *65*, 94. [CrossRef]
28. Wang, Z.; Yin, Y.; Yao, G.; Li, K.; Liu, Y.; Liu, X.; Tang, Z.; Zhang, F.; Peng, X.; Lin, J.; et al. BoilerNet: Deep reinforcement learning-based combustion optimization network for pulverized coal boiler. *Energy* **2025**, *318*, 134804. [CrossRef]
29. Zhang, Z.; Hu, J.; Wang, Y.; Pan, M.; Lu, K.; Ye, Y.; Yin, Z. An artificial intelligence-based strategy for multi-objective optimization of diesel engine fueled with ammonia-diesel-hydrogen blended fuel. *Energy* **2025**, *318*, 134701. [CrossRef]
30. Ren, S.; An, Y.; Pu, Y.; Liu, Y.; Lou, C.; Lim, M. Online prediction of combustion temperature field in a furnace from operating parameters and multi-point temperature data. *Energy AI* **2025**, *21*, 100530. [CrossRef]
31. Cao, Y.; Du, Z.; Hu, Z.; Jin, S.; Lu, W.; Zhang, R. The effects of the size and location of the recirculation windows of combustion chambers in a coke oven on emissions of NO and unburnt fuels by CFD numerical simulation. *IOP Conf. Ser. Mater. Sci. Eng.* **2020**, *964*, 12006. [CrossRef]
32. Zhang, A.Q.; Feng, Y.H.; Zhang, X.X.; Wang, M.D.; Yang, J.F.; Xu, Y. Decoupling simulation of thermal processes in coupled combustion and coking chambers of a coke oven. *ISIJ Int.* **2013**, *53*, 995–1001. [CrossRef]
33. Smith, D.; Frenklach, M.; Moriarty, N.; Eiteneer, B.; Goldenberg, M.; Bowman, C.; Hanson, R.; Song, S.; Gardiner, W.; Lissianski, V.; et al. GRI-Mech 3.0. Available online: http://www.me.berkeley.edu/gri_mech/ (accessed on 30 July 2025).
34. Chang, Y.; Jia, M.; Liu, Y.; Li, Y.; Xie, M.; Yin, H. Application of a decoupling methodology for development of skeletal oxidation mechanisms for heavy n -alkanes from n -octane to n -hexadecane. *Energy Fuels* **2013**, *27*, 3467–3479. [CrossRef]
35. Chen, Y.; Jiang, H.; Li, C.; Jia, X.; Ghamisi, P. Deep feature extraction and classification of hyperspectral images based on convolutional neural networks. *IEEE Trans. Geosci. Remote Sens.* **2016**, *54*, 6232–6251. [CrossRef]
36. Wang, X.; Chen, S.; Chen, L.; Zhu, D.; Liu, Y.; Wu, T. A hybrid MLP-CNN model based on positional encoding for daytime radiative cooler. *Opt. Commun.* **2024**, *560*, 130448. [CrossRef]
37. Nguyen, A.; Pham, K.; Ngo, D.; Ngo, T.; Pham, L. An analysis of state-of-the-art activation functions for supervised deep neural network. In Proceedings of the 2021 International Conference on System Science and Engineering (ICSSE), Nha Trang, Vietnam, 26–28 August 2021; pp. 215–220. [CrossRef]
38. Nemati, M. A data-driven machine learning approach for turbulent flow field prediction based on direct computational fluid dynamics database. *J. Appl. Fluid Mech.* **2024**, *17*, 60–74. [CrossRef]
39. Mahima, R.; Maheswari, M.; Roshana, S.; Priyanka, E.; Mohanan, N.; Nandhini, N. A comparative analysis of the most commonly used activation functions in deep neural network. In Proceedings of the 2023 4th International Conference on Electronics and Sustainable Communication Systems (ICESC), Coimbatore, India, 6–8 July 2023; pp. 1334–1339. [CrossRef]
40. He, K.; Zhang, X.; Ren, S.; Sun, J. Deep residual learning for image recognition. In Proceedings of the 2016 IEEE Conference on Computer Vision and Pattern Recognition (CVPR), Las Vegas, NV, USA, 26 June–1 July 2016; pp. 770–778. [CrossRef]

41. Nieto, D.M.C.; Quiroz, E.A.P.; Lengua, M.A.C. A systematic literature review on support vector machines applied to regression. In Proceedings of the 2021 IEEE Sciences and Humanities International Research Conference (SHIRCON), Lima, Peru, 17–19 November 2021; pp. 1–4. [CrossRef]
42. Mat Deris, A.; Mohd Zain, A.; Sallehuddin, R. Overview of support vector machine in modeling machining performances. *Procedia Eng.* **2011**, *24*, 308–312. [CrossRef]
43. Loshchilov, I.; Hutter, F. Decoupled weight decay regularization. *arXiv* **2019**, arXiv:1711.05101. [CrossRef]
44. Zhou, P.; Xie, X.; Lin, Z.; Yan, S. Towards understanding convergence and generalization of AdamW. *IEEE Trans. Pattern Anal. Mach. Intell.* **2024**, *46*, 6486–6493. [CrossRef] [PubMed]
45. Xie, X.; Xie, M.; Moshayedi, A.J.; Noori Skandari, M.H. A hybrid improved neural networks algorithm based on L2 and dropout regularization. *Math. Probl. Eng.* **2022**, *2022*, 8220453. [CrossRef]
46. Kang, T. *Analysis of Factors Influencing Nitrogen Oxide Formation in Coke Ovens*; Report, ACRE Coking & Refractory Engineering Consulting Corporation(Dalian): Dalian, China, 2024.
47. Hu, Z. Numerical Simulation of NO_x Formation in a Combustion Chamber of a Coke Oven by Computation Fluid Dynamics. Master's Thesis, Shanghai Institute of Technology, Shanghai, China, 2013. Available online: https://kns.cnki.net/kcms2/article/abstract?v=SHX-2ztJhde3_jxXIla7D-3ddIOkfwyUszT0re2-NDW1nYB2HgYDrYPyWcuYp3Q3Vl1da0d0XH1HPec1Bn-m372I2A2MF7EoMYsYLToyshkNAN05cJx6iZ9E0FDtDX29htzFpQlTL84hQZFvY2ShqPdJ6F1U-jt-FWpjI4oyVKDXujcxoYfXGVPCN5Zng1tZ&uniplatform=NZKPT&language=CHS (accessed on 21 May 2019).
48. Jin, K.; Feng, Y.; Zhang, X.; Wang, M.; Yang, J.; Ma, X. Simulation of transport phenomena in coke oven with staging combustion. *Appl. Therm. Eng.* **2013**, *58*, 354–362. [CrossRef]
49. Terui, K.; Matsui, T.; Fukada, K.; Dohi, Y. Influence of temperature distribution in combustion chamber on coke cake discharging behavior. *ISIJ Int.* **2018**, *58*, 633–641. [CrossRef]
50. FuRui; Al-Absi, M.A.; Lee, H.J. Introduce a specific process of genetic algorithm through an example. In Proceedings of the 2019 International Conference on Information and Communication Technology Convergence (ICTC), Jeju Island, Republic of Korea, 16–18 October 2019; pp. 422–425. [CrossRef]

Disclaimer/Publisher's Note: The statements, opinions and data contained in all publications are solely those of the individual author(s) and contributor(s) and not of MDPI and/or the editor(s). MDPI and/or the editor(s) disclaim responsibility for any injury to people or property resulting from any ideas, methods, instructions or products referred to in the content.